


Cite this: *Chem. Sci.*, 2024, 15, 2898

All publication charges for this article have been paid for by the Royal Society of Chemistry

Customizing precise, tunable, and universal cascade charge transfer chains towards versatile photoredox catalysis†

Xian Yan, Jun-Hao Dong, Jing-Ying Zheng, Yue Wu and Fang-Xing Xiao *

The core factors dictating the photocatalysis efficiency are predominantly centered on controllable modulation of anisotropic spatial charge transfer/separation and regulating vectorial charge transport pathways. Nonetheless, the sluggish charge transport kinetics and incapacity of precisely tuning interfacial charge flow at the nanoscale level are still the primary dilemma. Herein, we conceptually demonstrate the elaborate design of a cascade charge transport chain over transition metal chalcogenide-insulating polymer-cocatalyst (TIC) photosystems *via* a progressive self-assembly strategy. The intermediate ultrathin non-conjugated insulating polymer layer, *i.e.*, poly(diallyl-dimethylammonium chloride) (PDDA), functions as the interfacial electron relay medium, and simultaneously, outermost co-catalysts serve as the terminal “electron reservoirs”, synergistically contributing to the charge transport cascade pathway and substantially boosting the interfacial charge separation. We found that the insulating polymer mediated unidirectional charge transfer cascade is universal for a large variety of metal or non-metal reducing co-catalysts (Au, Ag, Pt, Ni, Co, Cu, NiSe₂, CoSe₂, and CuSe). More intriguingly, such peculiar charge flow characteristics endow the self-assembled TIC photosystems with versatile visible-light-driven photoredox catalysis towards photocatalytic hydrogen generation, anaerobic selective organic transformation, and CO₂-to-fuel conversion. Our work would provide new inspiration for smartly mediating spatial vectorial charge transport towards emerging solar energy conversion.

Received 29th October 2023
Accepted 29th December 2023

DOI: 10.1039/d3sc05761e

rsc.li/chemical-science

1. Introduction

In recent years, photocatalysis technology has enabled emerging solar energy conversion, providing a promising and sustainable solution to the issues of energy crises and climate deterioration.^{1–3} More importantly, these photocatalysis products are key feedstock for accessing value-added chemicals.^{4,5} Despite the great promise of photocatalysis, its catalytic efficiency has still been far from satisfactory, predominantly ascribed to the low utilization of photons, inefficient photo-carrier separation rate and poor vectorial charge modulation.^{6–8} To surmount these obstacles, diverse strategies have thus been explored, such as metal or nonmetal element doping,⁹ photosensitization with narrow band gap semiconductors,¹⁰ or constructing heterostructures with other semiconductors with suitable energy level alignment.¹¹ Nevertheless, these studies mainly emphasize the net photoactivity enhancement, and deep understanding on precise interfacial charge transfer modulation remains challenging.

Light absorption, charge separation, and surface reactions constitute the core issues of photocatalysis.¹² In particular, fine tuning of photoinduced charge migration to ideal catalytically active sites represents the key step to drive photoredox catalysis, which is primarily dictated by elaborate interface configuration engineering at the nanoscale level.¹³ Fundamentally, elegant interface architecture design for modulated charge migration/separation over heterostructured photosystems should rationally consider the following crucial factors including intimate integration of ingredients for crafting clean interfaces, reasonable spatial positioning of reduction and/or oxidation co-catalysts in the interface regime, and exploring easily accessible strategies to optimize the interface configuration in a control fashion.^{14–16} Recent years have witnessed a cornucopia toward the construction of composite photosystems with well-defined hetero-interfaces for multifarious photocatalysis, but precise and exquisite interface modulation for smartly tailoring interfacial charge transport pathways at the microscopic scale has so far not yet been truly achieved.

In traditional cognition, solid non-conjugated insulating polymers in principle cannot participate in the charge transfer process by virtue of deficiency of π conjugation in the whole framework of the molecular backbone.¹⁷ Nonetheless, our previous studies have confirmed that some quintessential non-conjugated insulating polymers can actually function as

College of Materials Science and Engineering, Fuzhou University, New Campus, Fujian Province, 350108, China. E-mail: fxxiao@fzu.edu.cn

† Electronic supplementary information (ESI) available. See DOI: <https://doi.org/10.1039/d3sc05761e>

unexpected charge (electron or hole)-withdrawing mediators to trigger photoredox and photoelectrochemical reactions, although their molecular structure lack delocalized π electrons.^{18,19} Intriguingly, encapsulation of semiconductors with non-conjugated insulating polyelectrolytes (PEs) facilitates defect passivation, and more importantly, provides a robust, versatile, convenient, and emerging platform to couple with diverse building blocks *via* molecular interaction with a view to designing well-defined and tail-made interfaces in terms of the generic surface charge properties of non-conjugated insulating PEs.²⁰ In this regard, the merits of solid non-conjugated insulating PEs make them applicable as surface charge mediators, efficient charge transport regulators, and effective hetero-interface architects.^{21–23} Despite the sporadic endeavors visualized in the past few years, judiciously harnessing PE as an interim layer to synergistically cooperate with co-catalysts in constructing elegant interfaces in conjunction with long-range charge transfer chains toward multivariate photoredox catalysis has yet to be achieved. This would significantly reinforce our fundamental understanding on the essential and universal role of non-conjugated insulating polymers in tuning the interfacial charge transfer pathways.

Inspired by the above motivations, herein, we conceptually propose the rational design of a novel cascade charge transport chain *via* solid non-conjugated insulating PE over TMC@PDDA@M (M: Au, Ag, Pt, Ni, Co, Cu, NiSe₂, CoSe₂, CuSe) heterostructured photosystems by a progressive self-assembly tactic. We found that the ultrathin PDDA interim layer functions as an electron withdrawing “pump” to considerably activate the interfacial charge transfer impetus, unexpectedly stimulating the unidirectional photoelectrons transport from the TMC substrate to the terminal “electron reservoirs” afforded by multifarious reduction co-catalysts. Such peculiar charge flow characteristics endow the self-assembled TMC@PDDA@M photosystems with versatile and significantly enhanced photoredox catalysis towards photocatalytic hydrogen generation, anaerobic photocatalytic selective organic transformation, and photocatalytic CO₂-to-fuel conversion. Our work would push forward the prosperity of insulating polymer mediated precise interface engineering and tunable charge transfer modulation in heterogeneous photocatalysis.

2. Experimental section

2.1 Materials

All the materials were of analytical grade and used as received without further purification, and detailed information is provided in the ESI.†

2.2 Preparation of photocatalysts

Experimental procedures for preparing the different photocatalysts in this work are provided in the ESI.†

2.3 Characterization

The crystal structure was determined by X-ray diffraction (XRD, Miniflex600). Morphologies were visualized by field emission

scanning electron microscopy (FESEM, Supra55, Carl Zeiss) coupled with energy-dispersive spectroscopy (EDS) and transmission electron microscopy (TEM, Tecnai G2 F20). Fourier transform infrared (FTIR) spectra were recorded on an infrared spectrophotometer (TJ270-30A). Raman spectra were collected with a Raman spectrometer (Dxr-2xi, Thermo Scientific, America). UV-visible diffuse reflectance spectra (DRS) were recorded on a Cary50 (Varian, America) with the reflectance background from 200 to 800 nm. X-ray photoelectron spectra (XPS) were recorded on a photoelectron spectrometer (ESCALAB 250, Thermo Scientific, America), and the binding energy (BE) of the elements were calibrated with the BE of C 1s (284.80 eV). Zeta potential (ξ) measurements were performed by dynamic light scattering analysis (Zeta sizer Nano ZS-90). Time-resolved photoluminescence (TRPL) spectra were recorded on a FLS 920 fluorescence lifetime spectrophotometer (Edinburgh, Instruments, UK). The photoluminescence (PL) spectra were probed on a Varian Cary Eclipse spectrophotometer. Brunauer–Emmett–Teller (BET) specific surface area and N₂ adsorption experiments were performed on an ASAP 2460.

2.4 Photocatalytic hydrogen evolution

Photocatalytic hydrogen evolution measurements were conducted on an online photocatalytic water splitting system (Shimadzu GC-8A with an MS-5A column using argon as the carrier gas), and using a 300 W Xe lamp (PLS-SXE300D, Beijing Perfect Light co. Ltd, China) as the irradiation source equipped with a cut-off optical filter ($\lambda > 420$ nm). The same light source and configuration were used for the subsequent photocatalytic activity detection reactions. The specific operational information is provided in the ESI.†

2.5 Selective photocatalytic reduction performances

Photocatalytic reduction of nitroaromatics to amino compounds was performed in an anaerobic environment (inert atmosphere N₂) along with adding a hole scavenger. Photoreduction products were analyzed with a UV-vis absorption spectrophotometer (Thermal Genesis). The specific operational information is provided in the ESI.†

2.6 Selective photocatalytic oxidation performances

Photocatalytic selective oxidation of aromatic alcohols to aldehydes was performed in a 10 mL Pyrex glass bottle at room temperature. The products were analyzed with a gas chromatograph (Shimadzu, GC-2014C). The specific operational information is provided in the ESI.†

2.7 Photocatalytic CO₂ reduction

Photocatalytic CO₂ reduction products were analyzed with a gas chromatograph (Shimadzu, GC-2014C). The specific operational information is provided in the ESI.†

2.8 Photoelectrochemical (PEC) measurements

PEC measurements were carried out on an electrochemical workstation (CHI660E, CHI Shanghai, Inc.) with a conventional three-



electrode system and 0.5 M Na₂SO₄ aqueous solution (pH = 6.69) was utilized as the electrolyte. The three-electrode system is composed of Pt foil (1 cm × 1 cm) as the counter electrode, and Ag/AgCl electrodes as the reference electrode and working electrodes. The working electrodes were prepared on fluorine-doped tin oxide (FTO) glass that was cleaned by sonication in DI H₂O and ethanol for 30 min and dried at 60 °C in an oven. The boundary of the FTO glass was protected using Scotch tape. The specific operational information is provided in the ESI.†

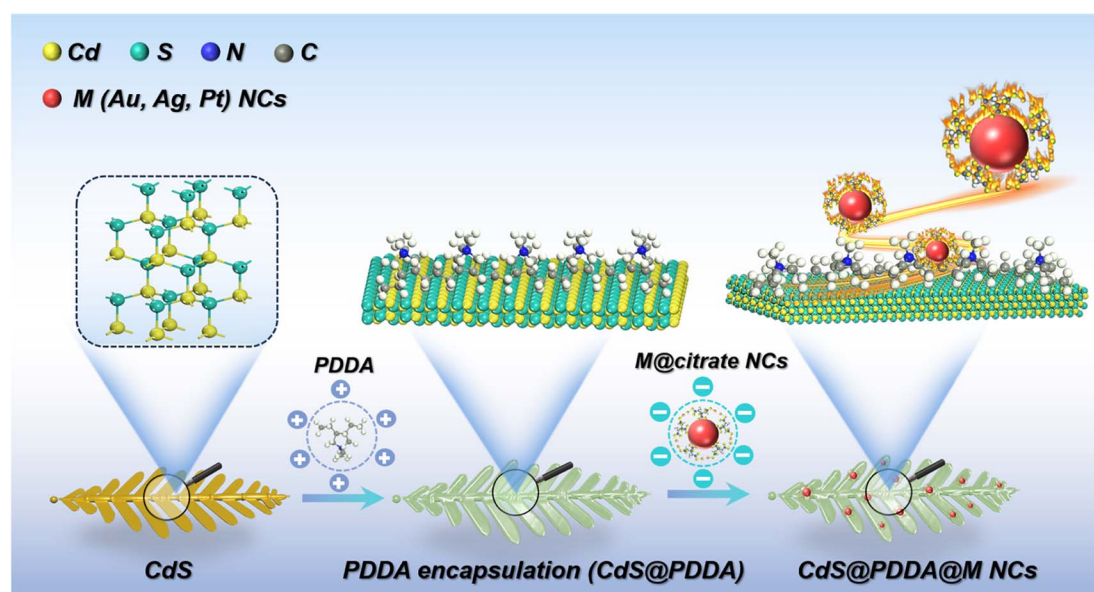
3. Results and discussion

3.1 Structural characterization

The detailed fabrication process of the CdS@PDDA@Au heterostructure is illustrated in Scheme 1. Specifically, CdS nano-leaves were firstly closely encapsulated with an ultrathin PDDA layer (positively charged unit) to generate a positively charged surface, which facilitates the attraction of oppositely charged Au@citrate nanocrystals (NCs) (negatively charged unit). Subsequently, coupling of positively charged CdS@PDDA with negatively charged Au@citrate NCs was achieved *via* a facile and efficient electrostatic self-assembly under ambient conditions, which gives rise to the multilayered CdS@PDDA@Au@citrate NCs (C@P@Au) ternary heterostructure. In this nanoarchitecture, ultrathin PDDA as an interface layer was integrated between CdS nano-leaves and Au@citrate NCs to form a sandwich structure. Similarly, considering the same citrate ligand, C@P@M (M: Ag@citrate, Pt@citrate) heterostructures were also prepared by the same principle. The accessibility of this ligand-initiated self-assembly process can be validated by the zeta potentials (ζ) of the assembly units (Fig. S1†).

X-ray diffraction (XRD) was used to characterize the crystal structures of these as-synthesized samples. Fig. 1a shows the XRD patterns of CdS, C@P15 and C@P15@Au7

heterostructures, and the diffraction peaks of CdS at 2θ of 24.90, 26.52, 28.28, 36.72, 43.83, 47.94 and 51.97° can be indexed to the (100), (002), (101), (102), (110), (103) and (112) crystal planes of hexagonal CdS (Fig. S2†) (PDF# 6-314). Analogously, these characteristic peaks are concurrently seen in the XRD patterns of C@P15 and C@P15@Au7 heterostructures, indicating no phase change of CdS after the PDDA encapsulation and Au@citrate NCs anchoring. In the XRD pattern of the C@P15@Au7 heterostructure, two diffraction peaks at 2θ of 38.14 and 64.76° assignable to the (111) and (220) crystal planes of cubic Au NCs (PDF# 2-1095) are observed, corroborating the anchoring of Au@citrate NCs in the C@P15 heterostructure. Note that the above mentioned two peaks are weak due to the relatively low loading amount of Au@citrate NCs, and it is also possible that the Au@citrate NCs peaks are shielded by the substantial peaks of the CdS substrate. Successful preparation of citrate-stabilized Au NCs can be further ascertained by the UV-vis absorption spectrum (Fig. S3†), wherein an apparent surface plasmon resonance (SPR) absorption band at 521 nm corresponding to Au NCs is clearly observed.²⁴ Fig. 1b and Table S1† show the FTIR spectra of CdS, C@P15 and C@P15@Au7 heterostructures, wherein the peaks at 2855 and 2923 cm⁻¹ in the FTIR spectra of C@P15 and C@P15@Au7 correspond to the -CH₂ groups from PDDA, corroborating encapsulation of PDDA on the CdS substrate.²⁵ As displayed in Fig. 1c, Raman spectra exhibit the featured peaks of CdS, and the peak intensity of C@P15 and C@P15@Au7 spectra shows a sequential weakening trend, which also corroborates the seamless PDDA encapsulation and Au@citrate NCs anchoring. The above analysis also confirms that our electrostatic self-assembly strategy developed to achieve the construction of heterostructures is efficient and accessible. Similarly, the difference in average pore size between CdS and C@P15@Au7 in the Brunauer-Emmett-Teller (BET) results also corroborates the above



Scheme 1 Schematic flowchart for the fabrication of CdS@PDDA@M NCs [C@P@M (M: Au, Ag, Pt)] heterostructures.



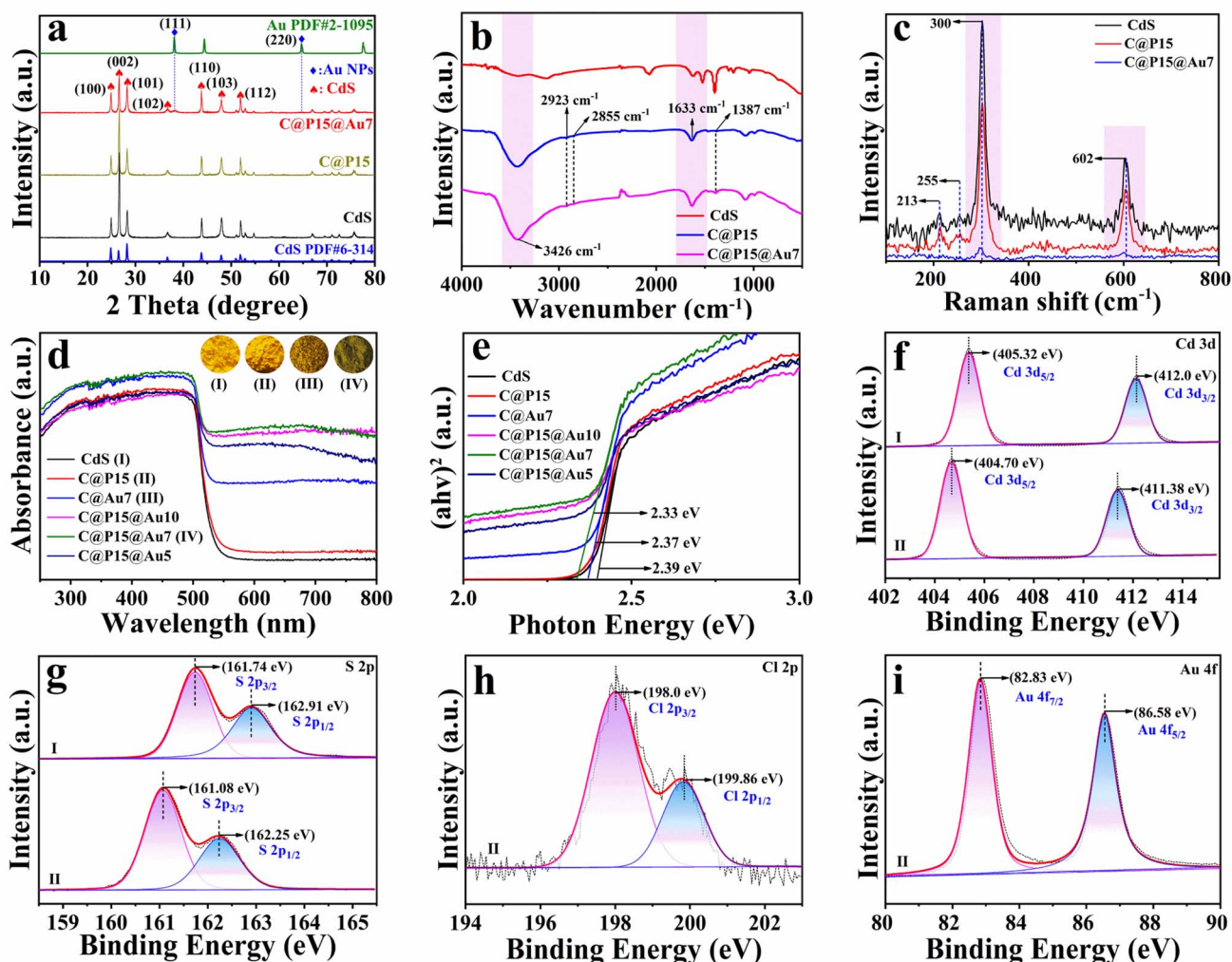


Fig. 1 (a) XRD patterns of CdS, C@P15 and C@P15@Au7 heterostructures, (b) FTIR spectra and (c) Raman of CdS, C@P15 and C@P15@Au7, and (d) DRS results of CdS, C@P15, C@Au7, C@P15@Au10, C@P15@Au7 and C@P15@Au5 with (e) transformed plots based on the Kubelka–Munk function vs. energy of light. High-resolution (f) Cd 3d, (g) S 2p, (h) Cl 2p and (i) Au 4f spectra of (I) pristine CdS and (II) C@P15@Au7.

speculation, wherein the average pore size of CdS and C@P15@Au7 is 6.548 and 7.214 nm, respectively (Fig. S4a, b† and Table S2†). In order to investigate the structural advantage and universality of the “sandwich layer” PDDA, we have also prepared some extension heterostructures such as C@M vs. C@P15@M (M: Ag, Pt)-7, C@M vs. C@P15@M (M: Ni, Co, Cu)-7 and C@X vs. C@P15@X (X: NiSe₂, CoSe₂, CuSe)-7 (Scheme S1†). The characterization of these heterostructures and Ag@citrate & Pt@citrate NCs is provided in Fig. S5, S6, S20 and S21,† respectively.

The optical properties of the samples were probed by UV-vis diffuse reflectance spectroscopy (DRS) to explore the light absorption capacity. As shown in Fig. 1d, all the samples demonstrate a characteristic absorption band edge at *ca.* 500 nm, and this stems from the inherent band-gap photoexcitation of the CdS substrate. Note that the CdS absorption band edge does not change after PDDA encapsulation, which stems from the fact that PDDA features an amorphous polymer with no optical response in the visible spectral domain, excluding its

possibility as a photosensitizer (Fig. S7†).²⁶ Similarly, citrate has no light response within the visible spectrum domain, thus ruling out its photosensitization effect (Fig. S8 and S10†). However, compared with pristine CdS and C@P15, C@Au7 and C@P15@Au (5, 7, 10) heterostructures exhibit remarkably enhanced light absorption in the visible region ranging from 500 to 800 nm, and meanwhile the absorption band edge presents a weak red shift, which is mainly attributed to the background absorption of Au@citrate NCs in the visible region (Fig. S3†). The band gaps (E_g) of the above samples were calculated using the following formula based on the Kubelka–Munk function:

$$(\alpha h\nu)^2 = A(h\nu - E_g) \quad (1)$$

where α , $h\nu$, and A denote the absorption coefficient, photon energy, and constant, respectively. In Fig. 1e, the bandgap values of CdS, C@Au7 and C@P15@Au7 are roughly determined to be 2.39, 2.33 and 2.39 eV, indicating that Au@citrate



NCs decoration does not cause substantial E_g variation for the CdS substrate. Although the ultrathin PDDA layer and Au@citrate NCs decoration do not substantially change the E_g of CdS, harmonious integration of PDDA and Au@citrate NCs on the CdS substrate using electrostatic self-assembly can effectively stimulate the photon capture in the visible light region by forming the heterostructures. It is noteworthy that the SPR band of Au (*ca.* 521 nm) is not observed in the DRS results of C@Au7 and C@P15@Au7, which is mainly ascribed to the overlapping absorption of the Au@citrate NCs with CdS substrate, thereby shielding the plasmonic peak of Au@citrate NCs.

With a view to revealing the cooperativity of Au@citrate NCs, PDDA and CdS, X-ray photoelectron spectroscopy (XPS) measurements were performed to unravel the elemental chemical states of the ingredients. The survey spectrum [Fig. S8a(II)†] of the C@P15@Au7 heterostructure unveils the presence of Cd, S, Au, C and Cl signals, among which Au is derived from Au@citrate NCs, C and Cl elements are from PDDA (Fig. S9†), and Cd and S elements originate from the CdS substrate. As displayed in the high-resolution Cd 3d spectrum of C@P15@Au7 [Fig. 1f(II)], the peaks situated at 404.70 (Cd 3d_{5/2}) and 411.38 eV (Cd 3d_{3/2}) are attributed to the Cd²⁺ species.²⁷ As revealed in Fig. 1g(II), the high-resolution S 2p spectrum of C@P15@Au7 with two peaks at 161.08 (S 2p_{3/2}) and 162.25 eV (S 2p_{1/2}) are ascribed to the S²⁻ species.²⁸ Perspicuously, the characteristic Cd and S peaks of C@P15@Au7 show significant shift toward lower binding energy compared to pristine CdS. Coincidentally, this interesting phenomenon also appears in the XPS results of extension heterostructure samples such as C@P15@Ag7, C@P15@Pt7, C@P15@Ni7, *etc.* (Fig. S11–S18†), implying that electronic interaction does occur among CdS, PDDA and Au@citrate NCs (Ag, Pt, *etc.*).²⁹ Deposition of an ultrathin PDDA layer on the CdS substrate is confirmed by the high-resolution Cl 2p spectrum (Fig. 1h), wherein the peaks at 198.0 (Cl 2p_{3/2}) and 199.86 eV (Cl 2p_{1/2}) belong to Cl⁻ species from PDDA.³⁰ Fig. 1i demonstrates two peaks in the high-resolution Au 4f spectrum of C@P15@Au7, in which the peaks at 82.83 (Au 4f_{7/2}) and 86.58 eV (Au 4f_{5/2}) point to the metallic Au species (*i.e.*, Au⁰).³¹ Consequently, XPS results (Table S3†) strongly corroborate that PDDA and Au@citrate NCs have been successfully self-assembled on the CdS substrate for the C@P15@Au7 heterostructure.

The morphologies and microstructures of the samples were studied by field-emission scanning electron microscopy (FESEM) and transmission electron microscopy (TEM). As shown in Fig. 2a and d, pristine CdS exhibits a clear and well-defined pinnate leaf-like structure with a pronounced trunk and highly ordered branches distributed on both sides of the trunk, wherein the dimension of the nano-leave is in the range of 4–6 μm . The CdS surface is smooth and composed of several parallel laminar layers with multiple steps. These unique nano-leaf structures not only expose a high density of active sites but also effectively shorten the vertical travel distance of the photogenerated carriers and thus inhibit the charge recombination over CdS.³² When CdS was encapsulated with a PDDA layer, as revealed in Fig. 2b, the morphology of C@P15 is not altered

compared with that of CdS, which is due to the ultrathin thickness of the PDDA layer, making a clear differentiation of them merely from FESEM images rather difficult. As displayed in Fig. 2c, C@P@Au7 exhibits an apparently rough surface that is different from the morphology of CdS and C@P15, manifesting deposition of Au@citrate NCs on the CdS substrate with the help of PDDA by electrostatic self-assembly. Fig. 2e shows the HRTEM image of pristine CdS, whose designated area exhibits a clear crystalline structure with a distinguishable lattice fringe of *ca.* 0.358 nm, corresponding to the (100) crystal facet of hexagonal CdS. In order to obtain more information on the ultrathin PDDA layer encapsulation on the CdS substrate, the HRTEM image of C@P15 is presented. Similarly, as shown in Fig. 2f, a clear lattice stripe with a lattice fringe of *ca.* 0.209 nm is obviously observed, which is attributed to the (110) crystal facet of hexagonal CdS. As marked by the yellow dotted line, it is apparent that an amorphous PDDA layer is closely and uniformly tethered on the outermost surface of the CdS substrate. Moreover, PDDA encapsulation on the CdS can also be corroborated by the EDX and elemental mapping results of C@P15, as displayed in Fig. S19a† and 2j. Among them, N and Cl signals originating from PDDA can be clearly observed, verifying that the PDDA layer is successfully encapsulated on the CdS substrate. In particular, as reflected by Fig. 2j4 and 5, the signal distribution patterns of N and Cl elements exhibit a nano-leaf framework, which once again more intuitively verifies that the PDDA layer is seamlessly coated on the whole skeleton of CdS nano-leaves. The intimate integration of Au@citrate NCs with CdS@PDDA15 is unveiled by the TEM image in Fig. 2g, in which Au@citrate NCs are uniformly and closely anchored on the C@P15 nano-leaves with the aid of electrostatic driving force. The mean diameter of Au@citrate NCs is about 14.01 nm (Fig. S20†). Fig. 2h and i show the HRTEM images of C@P15@Au7, wherein an ultra-thin PDDA layer is integrated between CdS and Au@citrate NCs, with visible lattice stripes of *ca.* 0.358 and 0.236 nm corresponding to the (100) and (111) crystal planes of hexagonal CdS and cubic Au NCs, respectively. EDS and TEM elemental mapping results in Fig. S19b† and 2k confirm the co-existence of Cd, S, C, Au, N, and Cl elements, implying that CdS, PDDA and Au@citrate NCs are concurrently integrated in the C@P15@Au7 heterostructure. The above analysis is also consistent with the previous XPS results. Similarly, EDS and FESEM mapping results of C@P15@Au7 (Fig. S23†) and extension heterostructures (Fig. S24–S31†) also point to the analogous conclusion.

3.2 Photocatalytic reduction activities

The photocatalytic hydrogen generation performances of the samples under visible light irradiation ($\lambda > 420$ nm) were probed to unlock the synergistic contribution of CdS, PDDA and Au@citrate NCs in boosting the solar-to-hydrogen conversion efficiency.³³ As shown in Fig. 3a, pristine CdS exhibits a low photocatalytic H₂ evolution rate of 6.814 mmol h⁻¹ g⁻¹ under visible light irradiation, and this is mainly due to its intrinsic photo-corrosion and built-in electric field limitation. After ultra-



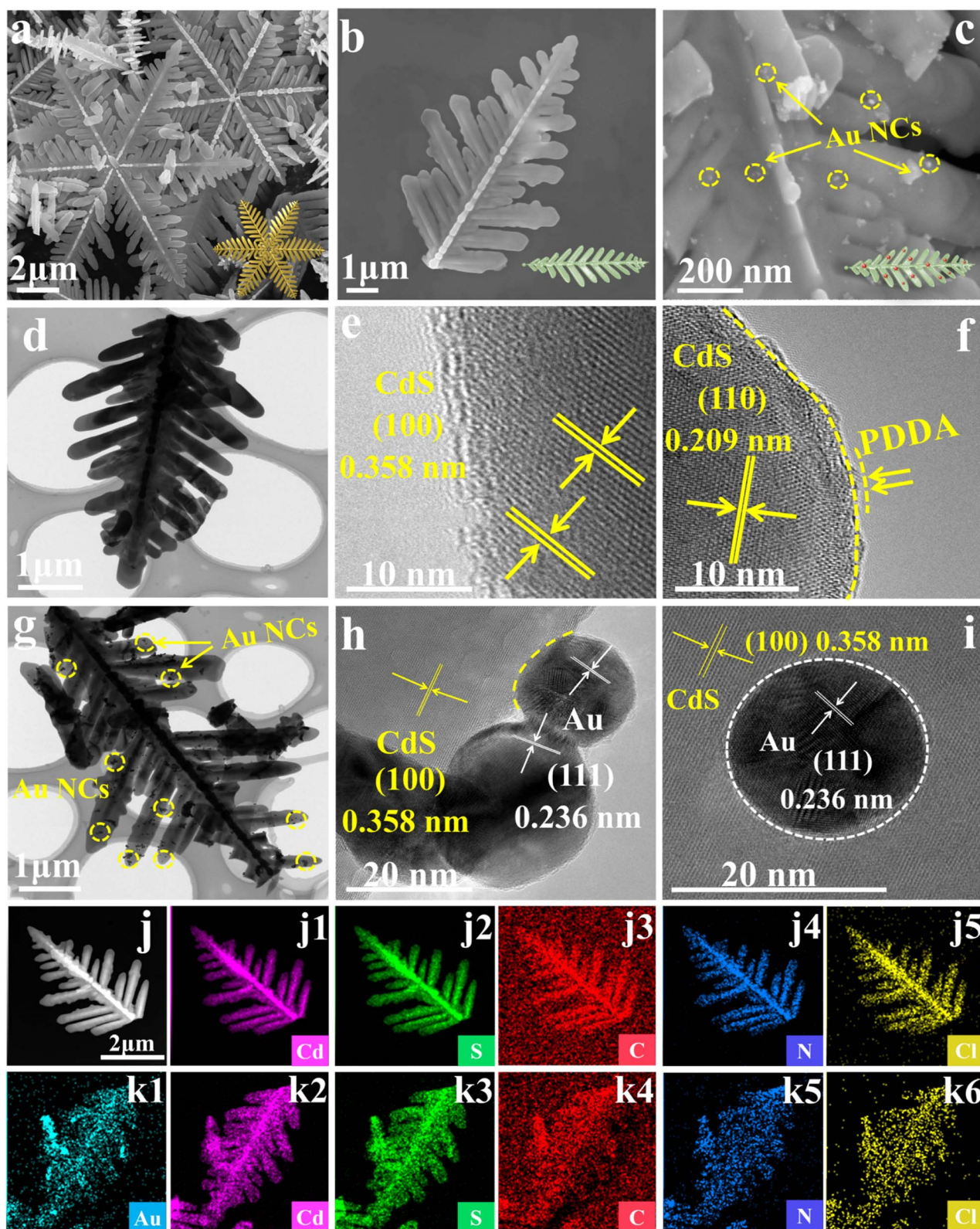


Fig. 2 (a–c) FESEM images of CdS, C@P15 and C@P15@Au7 with schematic models in the inset, low-magnification TEM images of (d and g) CdS and C@P15@Au7 with schematic models in the inset, HRTEM images of (e) CdS, (f) C@P15 and (h–i) C@P15@Au7, and elemental mapping results of (j) C@P15 and (k) C@P15@Au7.



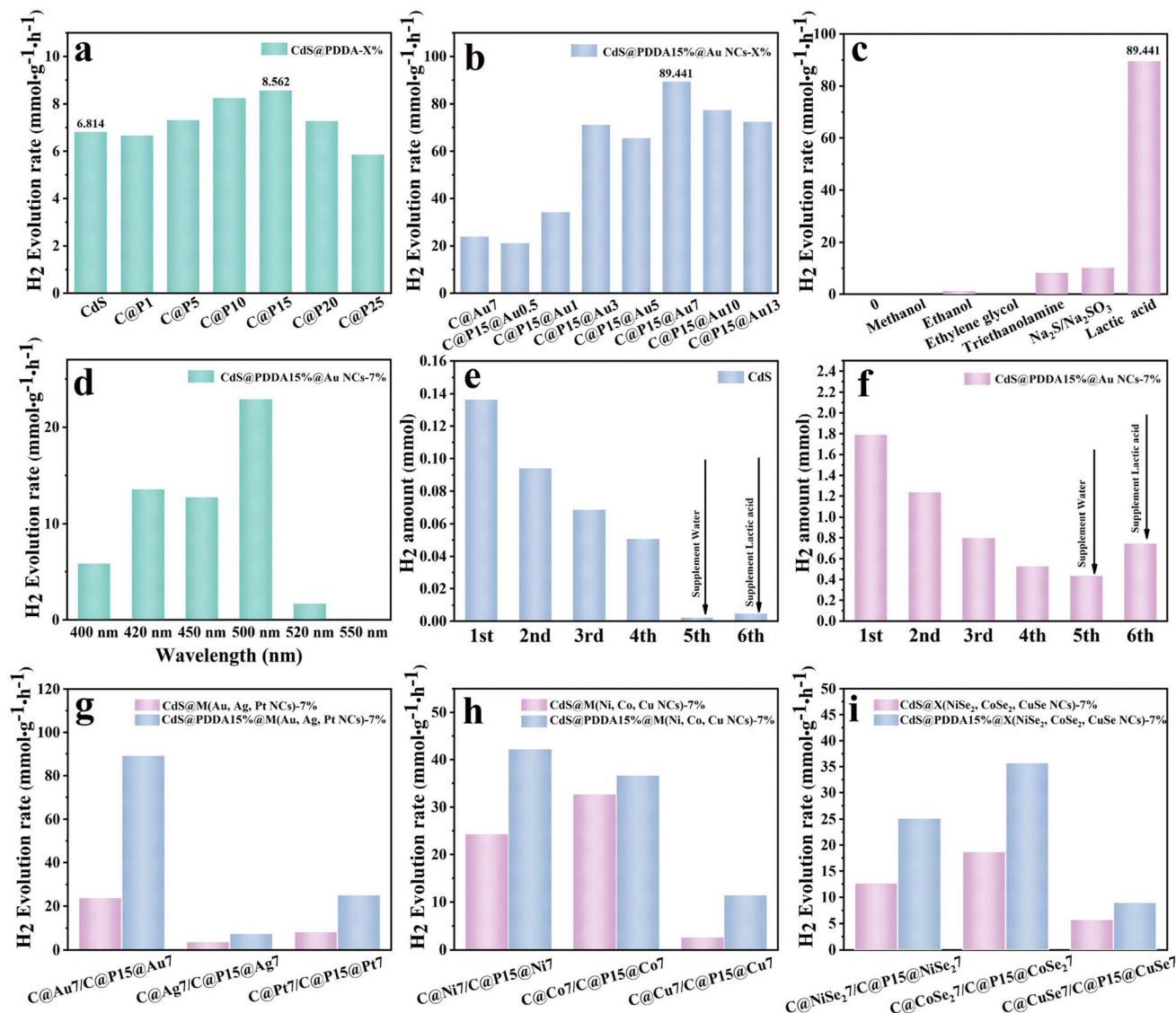


Fig. 3 (a) Photocatalytic H₂ evolution performances of CdS and C@P-X% (X: 1, 5, 10, 15, 20, 25) with different mass ratios of PDDA under visible light ($\lambda > 420$ nm) irradiation, (b) photocatalytic hydrogen evolution rates of C@P15@Au-X% (X: 0.5, 1, 3, 5, 7, 10, 13, 16) heterostructures with different mass ratios of Au@citrate NCs, (c) photocatalytic hydrogen evolution rates of C@P15@Au7 in the presence of different sacrificial reagents, and (d) under different monochromatic light irradiation, (e and f) photocatalytic cyclic reaction of blank CdS and C@P15@Au7 and (g–i) photocatalytic hydrogen production rates of extension heterostructures including C@M vs. C@P15@M (M: Au, Ag, Pt)-7, C@M vs. C@P15@M (M: Ni, Co, Cu)-7 and C@X vs. C@P15@X (X: NiSe₂, CoSe₂, CuSe)-7.

thin PDDA encapsulation, the photocatalytic hydrogen generation rate of C@P shows an increasing trend and then decreases with increasing the PDDA encapsulation amount. Perspicuously, ultrathin PDDA coating on the CdS substrate contributes to boosted photocatalytic H₂ evolution performance but this is closely related to the PDDA amount. On the basis of the systematic investigation, C@P15 is determined as the optimal sample with the photocatalytic H₂ evolution rate reaching 8.562 mmol g⁻¹ h⁻¹. Technically, efficient separation and directional photoelectron migration are the essential prerequisites for photocatalytic H₂ evolution. Since PDDA fails to serve as a photosensitizer (Fig. S7†), photoelectron generation of the C@P heterostructure still depends on the intrinsic band-gap-

photoexcitation of the CdS substrate. In view of the enhanced H₂ evolution activity of C@P, it is certain that PDDA plays an active role in promoting the directional migration of photoelectrons.³⁴ Over-coating PDDA on the CdS leads to reduced photoactivity, which is probably caused by the fact that thicker PDDA coating increases the electron transport distance.

In order to judiciously harness the pivotal role of PDDA in mediating interfacial charge transfer, Au@citrate NCs were chosen as the electron traps to construct a ternary heterostructure with a fine interface (*i.e.*, C@15P@Au) by electrostatic self-assembly in conjunction with exploring its H₂ evolution activity. As displayed in Fig. 3b, the photocatalytic H₂ evolution rates of C@P15@Au-X% (X: 0.5, 1, 3, 5, 7, 10, 13, 16) are heavily

dependent on the Au@citrate NCs loading amount, among which C@P15@Au7 exhibits an optimal hydrogen evolution rate of $89.441 \text{ mmol g}^{-1} \text{ h}^{-1}$, far exceeding those of the pristine CdS and C@Au7 counterparts. The significant difference in H_2 evolution performance between C@Au7 and C@P15@Au7 indicates that introducing the PDDA interfacial layer can accelerate electron transfer between the CdS substrate and Au@citrate NCs. Furthermore, we have performed contact angle tests for CdS, C@P15@Au7 and C@Au7 samples, as shown in Fig. S32.† Obviously, the three samples are all hydrophilic materials with contact angles close to $12\sim 16^\circ$. In order to more clearly ascertain the pivotal role of the PDDA interim layer in constructing accelerated electron transfer channels, the C@P15@Au7 photocatalyst was calcined at high temperature to remove PDDA and then used as a control sample to evaluate its photocatalytic H_2 evolution activity. The thermogravimetric analysis (TGA) curve of C@P15@Au7 was recorded under a nitrogen atmosphere. As shown in Fig. S33,† a substantial weight loss is observed between 250 and 450°C in the TGA curve of C@P15@Au7, which is mainly due to the gradual decomposition of PDDA as the calcination temperature increases. Fig. S34† shows the H_2 evolution performance of CdS vs. CdS- 450°C , C@Au7 vs. C@Au7- 450°C and C@P15@Au7 vs. C@P15@Au7- 450°C heterostructures. The H_2 evolution activities of CdS and C@Au7 only change slightly before and after calcination, corroborating that the high-temperature calcination process does not significantly compromise the photoactivity of CdS and Au@citrate NCs. However, unexpectedly, the photocatalytic H_2 evolution rate of C@P15@Au7- 450°C is far inferior to that of the original C@P15@Au7, strongly confirming that PDDA indeed plays a crucial role in accelerating the interfacial directional electron migration.

As mirrored in Fig. 3c, the photocatalytic H_2 evolution rate of C@P15@Au7 is considerably influenced by the type of sacrificial reagent, among which lactic acid demonstrates the optimal efficiency owing to its high deprotonation efficiency.³⁵ Fig. 3d reveals the photocatalytic H_2 evolution rates of C@P15@Au7 at different excitation wavelengths, which reveals optimal hydrogen evolution activity at an incident wavelength of 500 nm . Note that the action spectrum is in good agreement with the DRS result, implying the predominant role of band-gap-photoexcitation of the CdS substrate. To elaborate the influence of light absorption on the photocatalytic H_2 evolution activity, the wavelength-dependent apparent quantum yield (A.Q.Y) of C@P15@Au7 was probed (Fig. S35 and Table S7†). Apparently, C@P15@Au7 exhibits the highest A.Q.Y efficiency of 26.91% at 450 nm , indicating that the photocatalytic H_2 evolution reaction of C@P15@Au is truly driven by the intrinsic photoexcitation of the CdS substrate. Apart from the outstanding photoactivity, excellent stability is also an important indicator for evaluating excellent photocatalysts. The cyclic photocatalytic H_2 evolution performances of CdS and C@P15@Au7 under visible light irradiation were probed by performing six consecutive photocatalytic reactions with each cycle lasting for 2 h . As displayed in Fig. 3e and f, the photocatalytic H_2 evolution activities of both CdS and C@P15@Au7 show varying degrees of decay after several sets of cyclic

reactions, among which the CdS attenuation was the most severe. To investigate the key factors restricting the photocatalytic hydrogen evolution stability of CdS and C@P15@Au7, controlled experiments were performed after four sets of cycles with supplementing solvent (water) and a hole trapping agent (lactic acid) as the modulating variables. After the above adjustment, the photocatalytic hydrogen evolution activity of CdS still shows a substantial decay. Obviously, the hydrogen evolution activity decay of CdS under continuous light irradiation is inevitable, which is caused by its inherent photo-corrosion (Fig. S36a†). Intriguingly, as displayed in Fig. 3f, the photocatalytic H_2 evolution activity of C@P15@Au7 shows a significant recovery after supplementing the electron donor (lactic acid). Thus, it can be speculated that the decrease in the photocatalytic H_2 evolution activity of C@P15@Au7 after continuous light irradiation may be caused by the consumption of the sacrificial reagent. Additionally, we have characterized C@P15@Au7 after cyclic photoreactions using XRD, XPS, FTIR SEM, and TEM to more comprehensively dissect the factors influencing the stability of the photocatalyst. Consistently, the XRD (Fig. S37a†), FTIR (Fig. S37b†) and XPS (Fig. S38†) results of C@P15@Au7 after cyclic reactions are not altered, and the results agree well with those of the freshly prepared counterpart. Fig. S39a and b† show the FESEM and low-magnification TEM images of C@P15@Au7 after cyclic photoreactions, respectively. Obviously, the continuous stirring during the cyclic reactions causes the fragmentation of the CdS nano-leaves, and the substantial accumulation of these CdS fragments inevitably leads to the shielding of active sites, thus inhibiting the photoactivity. Fig. S39g† displays the element mapping results of C@P15@Au7 after cyclic photoreactions. Upon the CdS nano-leaf skeleton, the Au@citrate NCs are observed to be sparsely distributed, which is due to the destruction of surface citrate ligands during the photoreaction process, causing the Au@citrate NCs to detach from the CdS nano-leaves. This is also one of the reasons for the poor stability of the photocatalysts. In summary, fine interface engineering over the C@P15@Au heterostructure constructed by electrostatic self-assembly affords efficient photoactivity, and introducing an interfacial electron-withdrawing medium (PDDA) favors the construction of a characteristic electron transport channel.

Besides C@P15@Au7, with a view to evaluating the universality of PDDA in mediating electron transfer, we also prepared other heterostructures and evaluated their photocatalytic H_2 evolution activities. Since the photoelectrons originate from the photoexcitation of the CdS substrate, the universality of PDDA can be keenly detected by replacing the outermost electron acceptors. As displayed in Fig. 3g–i, the photocatalytic H_2 evolution trend of these heterostructures follows the order of C@P15@M7 (M: Ag, Pt, Ni, Co, Cu) > C@M7 (M: Ag, Pt, Ni, Co, Cu) and C@P15@X7 (X: NiSe_2 , CoSe_2 , CuSe) > C@X7 (X: NiSe_2 , CoSe_2 , CuSe). Obviously, alternative electron acceptors whether from precious metal NCs to non-precious metal or to the semiconductor, PDDA, can always trigger the synergistic effect by accelerating the directional electron transfer.



Apart from the photocatalytic H_2 evolution reaction, aromatic nitro compounds with more stringent triggering conditions (6 electrons) were selected for selective photoreduction to verify the universality of the PDDA mediated electron transport model (Fig. 4l). The photoactivities of the samples were evaluated by anaerobic photocatalytic reduction of aromatic nitro compounds to amino derivatives under visible light irradiation ($\lambda > 420$ nm) with the addition of ammonium formate as a hole quencher and N_2 bubbling under ambient conditions, which makes electrons the only active species during the reaction. Fig. 4a shows the photoactivities of the CdS substrate, C@Au7 and C@P15@Au7 heterostructures under visible light irradiation, from which it is apparent to see that C@P15@Au can fulfil the photoreduction of 4-nitroaniline (4-NA) to 4-phenylenediamine (4-PDA) within 100 s, far exceeding the blank CdS and C@Au7 counterparts. To gain insight into the decisive role of photogenerated electrons in triggering the photoreduction performance of C@P15@Au7, controlled experiments were conducted by adding AgNO_3 as the electron scavenger. As exhibited in Fig. S40,† C@P15@Au7 exhibits negligible photoactivity with adding AgNO_3 for electron quenching. Similarly, in a controlled experiment, the photoreduction conversion rate of C@P15@Au7-450 °C is also substantially reduced (Fig. S41†). Obviously, as the core species of the photoreduction reaction, targeted photoelectron migration to the active site is essential to drive the photoreduction reaction. Based on the above analysis, although the triggering conditions of the photoreduction reaction are harsher than those of the photocatalytic hydrogen evolution reaction, PDDA still shows powerful electron transport potential in the photocatalytic selective organic transformation reaction.

In order to further highlight the general role of PDDA in mediating photoreduction reactions, apart from 4-NA (Fig. 4a), a series of nitroaromatics including 3-nitroaniline (3-NA), 2-nitroaniline (2-NA), 3-nitrophenol (3-NP) and 2-nitrophenol (2-NP) were also utilized as the substrates for selective photoreduction catalysis (Fig. 4b–e). Consistently, C@P15@Au7 still maintains the significant photoreduction advantage in these reactions compared with CdS and C@Au7. In addition to the generalized photoreduction experiments of nitroaromatic species, we also performed a 4-NA photoreduction probe reaction based on a series of PDDA-mediated heterostructures (C@M vs. C@P15@M and C@X vs. C@P15@X). Analogous photoreduction trends have also been observed in these extended heterostructure based photosystems (Fig. 4f–k).

Compared with the photocatalytic hydrogen evolution and aromatic nitro compound reduction reactions, photocatalytic CO_2 reduction is a multi-electron involved reaction that results in the formation of multiple intermediate molecules, making the products diverse, and moreover, the chemical inertness of CO_2 makes the reaction more complex.^{36,37} Under such harsh triggering conditions, we probed the photocatalytic CO_2 reduction performance of the C@P15@Au7 heterostructure to unveil whether PDDA can still function as a powerful charge transport mediator. The photocatalytic CO_2 reduction activities of the samples were explored under visible light irradiation ($\lambda > 420$ nm) with triethanolamine (TEOA) as the hole quencher. As displayed in Fig. 5a, the

photoreduction rate of CO_2 to CO over C@P15@Au7 is enhanced by 9.1 and 2.9 times relative to those over blank CdS and C@Au7, respectively. As a controlled experiment, the CO evolution rate of C@P15@Au7 is 5.3 times larger than that of C@P15@Au7-450 °C (Fig. S42†). Apparently, utilizing PDDA as the electron transport mediator, C@P15@Au7 exhibits the most considerably enhanced photoactivity with respect to CdS and C@Au7, confirming the previous presumption and universal role of PDDA. In addition, an isotopic tracer experiment is carried out to identify the origin of the carbonaceous products.³⁸ The overwhelming signals of $m/z = 29$ and $m/z = 17$ originating from the $^{13}\text{CO}_2$ carbon source indicate that the obtained carbon products (CH_4 and CO) are derived from CO_2 rather than any other impurities (Fig. 5b).³⁹ Furthermore, we carried out cyclic experiments (Fig. 5c) and found that C@P15@Au7 still exhibits retained photocatalytic activity after seven runs (*i.e.*, 14 h in total), which proves the favorable stability of C@P15@Au7. Finally, a series of universal experiments (Fig. 5d–i) manifest that the ultrathin PDDA interim layer as an electron transport mediator can not only match different electron collectors (Ag, Pt, Ni, Co, NiSe_2 , and CoSe_2) but also still show inexhaustible electron transport capability.

3.3 Photocatalytic oxidation activities

Apart from photocatalytic hydrogen evolution, selective reduction of aromatic nitro compounds and CO_2 reduction, photocatalytic selective oxidation of aromatic alcohols to the corresponding aldehydes was also carried out. As shown in Fig. S43,† the C@P15@Au7 heterostructure exhibits substantially enhanced visible-light-driven photoactivity toward the oxidation of aromatic alcohols to aldehydes with high conversion and yield. In contrast, CdS and C@Au7 exhibit very poor photoactivity in terms of conversion and yield, which is reasonable considering the ultrafast carrier recombination rate of CdS and C@Au7. As expected, the interfacial PDDA interim layer in the C@P15@Au7 heterostructure can effectively boost the carrier separation rate, which is beneficial to the conversion of alcohols to aldehydes. Furthermore, the dominant active species responsible for the photocatalytic oxidation of aromatic alcohols to aldehydes over the C@P15@Au7 heterostructure were determined by quenching experiments through adding different scavengers. Among them, benzoquinone (BQ), potassium persulfate ($\text{K}_2\text{S}_2\text{O}_8$), *tert*-butylalcohol (TBA), and Na_2SO_3 were added into the reaction system to quench superoxide radicals (O_2^-), electrons (e^-), hydroxyl radicals (OH^\bullet) and holes (h^+), respectively. Besides, a controlled experiment with N_2 purge was performed to unveil the effect of dissolved O_2 on photoactivity. As manifested in Fig. S44,† the photoactivity of C@P15@Au7 utilizing N_2 -saturated BTF solvent is markedly lower than that utilizing O_2 -saturated BTF solvent, which is understandable because dissolved O_2 is beneficial for the production of O_2^- , OH^\bullet and other oxygen-containing active species, which significantly influence the efficiency of photocatalytic reactions. The above conclusion is also confirmed by the control reaction for quenching of O_2^- and OH^\bullet radicals. Also, introducing $\text{K}_2\text{S}_2\text{O}_8$ as an electron scavenger also causes similar photoactivity inhibition, which can be ascribed to the fact that electron quenching retards the formation of O_2^- and OH^\bullet active species. The correlation of



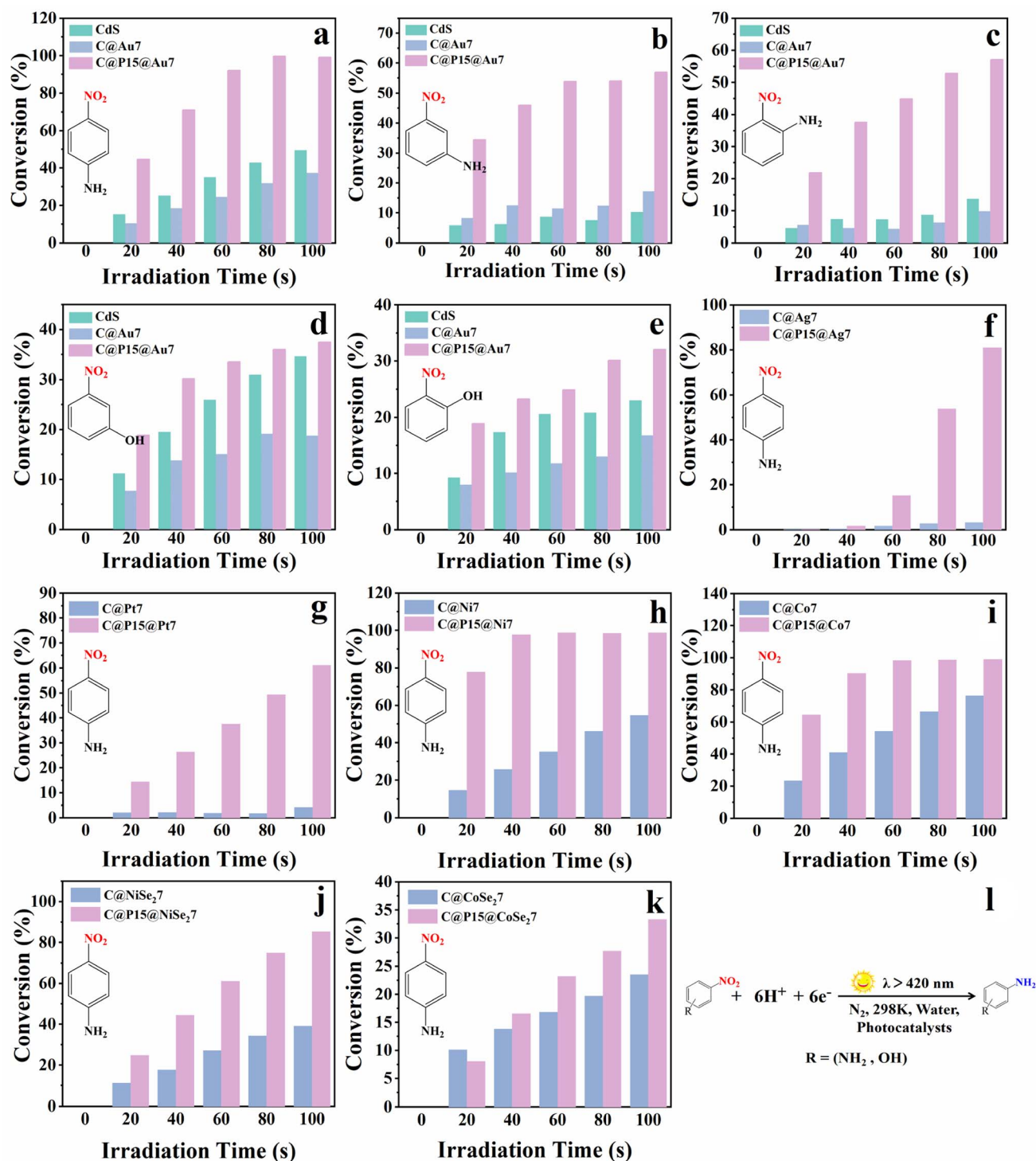


Fig. 4 Photocatalytic performances of CdS, C@Au7 and C@P15@Au7 heterostructures toward selective reduction of nitroaromatics under visible light irradiation ($\lambda > 420$ nm) with the addition of ammonium formate as a hole scavenger and N₂ bubbling under ambient conditions including (a) 4-NA, (b) 3-NA, (c) 2-NA, (d) 3-NP, and (e) 2-NP and (f–k) photoreduction of 4-NA of extension heterostructures including C@M vs. C@P15@M (M: Ag, Pt)–7, C@M vs. C@P15@M (M: Ni, Co)–7 and C@X vs. C@P15@X (X: NiSe₂, CoSe₂)–7, and (l) typical reaction model under the current experimental conditions.

electrons with the formation of $\cdot\text{O}_2^-$ and $\cdot\text{OH}$ radicals is demonstrated by formulae (2)–(4) below. Similarly, a control experiment with adding Na₂SO₃ in the reaction system also confirms that holes

play an important role in promoting the photoactivity of C@P15@Au7. Based on the above analysis, contributing roles of these active species follow the order of $\cdot\text{OH} > e^- > \cdot\text{O}_2^- > h^+$. These



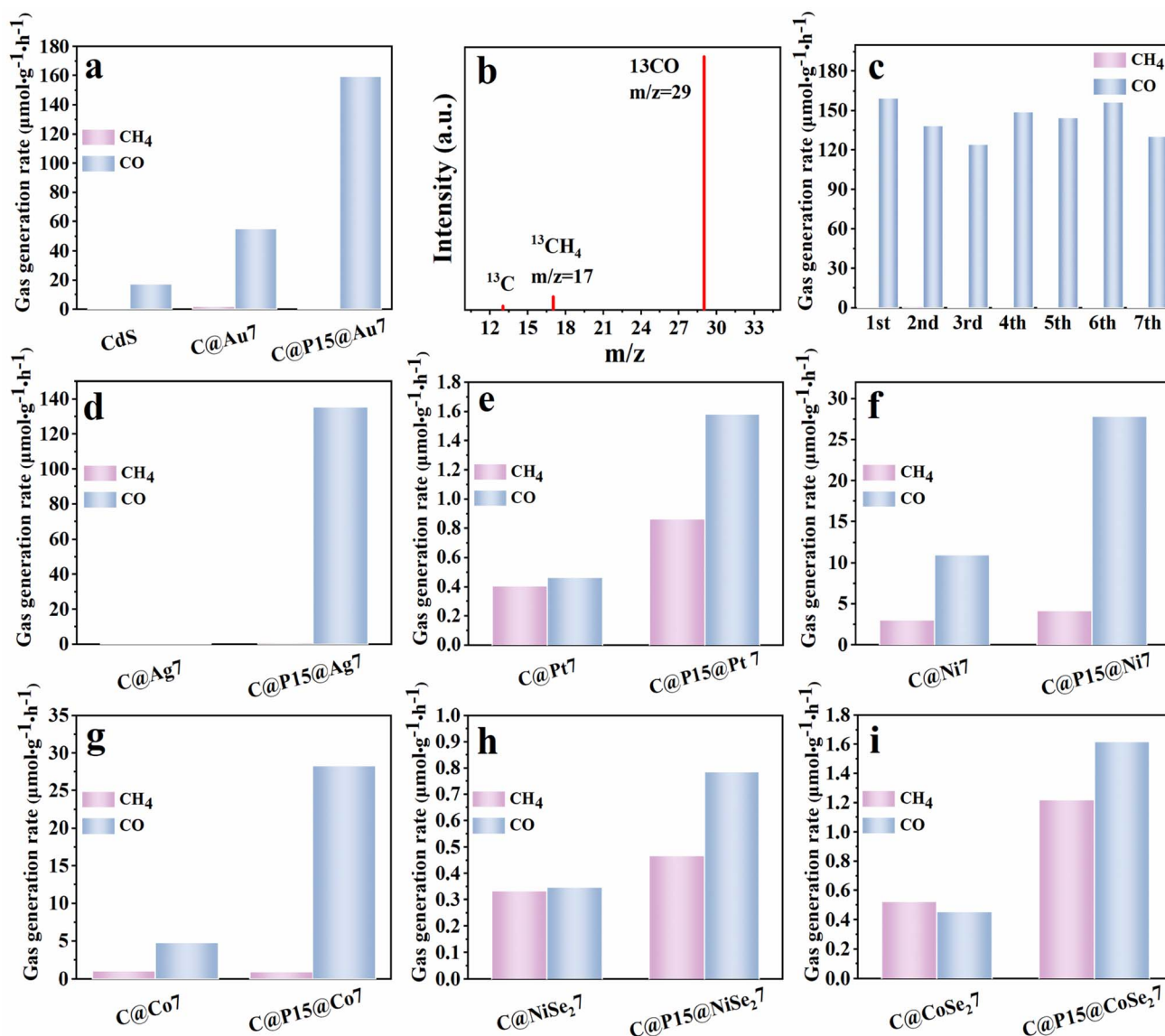
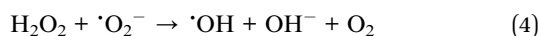
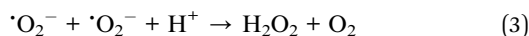


Fig. 5 (a) Photocatalytic CO₂ reduction performances of CdS, C@Au7 and C@P15@Au7 heterostructures under visible light ($\lambda > 420$ nm) irradiation, (b) CO and CH₄ products generated from the ¹³CO₂ isotope experiments, (c) photocatalytic cyclic reaction of C@P15@Au7 and (d–i) photocatalytic CO₂ reduction performances of extension heterostructures including C@M vs. C@P15@M (M: Ag, Pt)–7, C@M vs. C@P15@M (M: Ni, Co)–7 and C@X vs. C@P15@X (X: NiSe₂, CoSe₂)–7.

results strongly signify the general role of PDDA in photoredox catalysis for improving the charge migration and separation.



3.4 PEC and spectroscopic analysis

Photoelectrochemical (PEC) measurements were carried out to evaluate the separation efficiency of photoinduced electron–hole pairs over the different samples. Transient photocurrent response is considered to be the most intuitive means to

evaluate the efficiency of carrier separation at the photo-electrode.^{40,41} Fig. 6a shows the periodic on/off transient photocurrent response of C@Au7 and C@P15@Au7 heterostructures under intermittent visible light irradiation ($\lambda > 420$ nm), from which it is apparent that the photocurrent density of C@P15@Au7 is much larger than that of C@Au7. The great disparity of photocurrent density indicates that embedding of an interfacial PDDA interim layer can indeed accelerate the interfacial electron transport to improve the carrier separation efficiency, which is consistent with the photocatalytic performance analysis aforementioned. Electrochemical impedance spectroscopy (EIS), as a simple method to monitor the charge transfer process on the electrode and at the contact interface between the electrode and electrolyte,⁴² has further confirmed that C@P15@Au7 embedded with an ultrathin intermediate

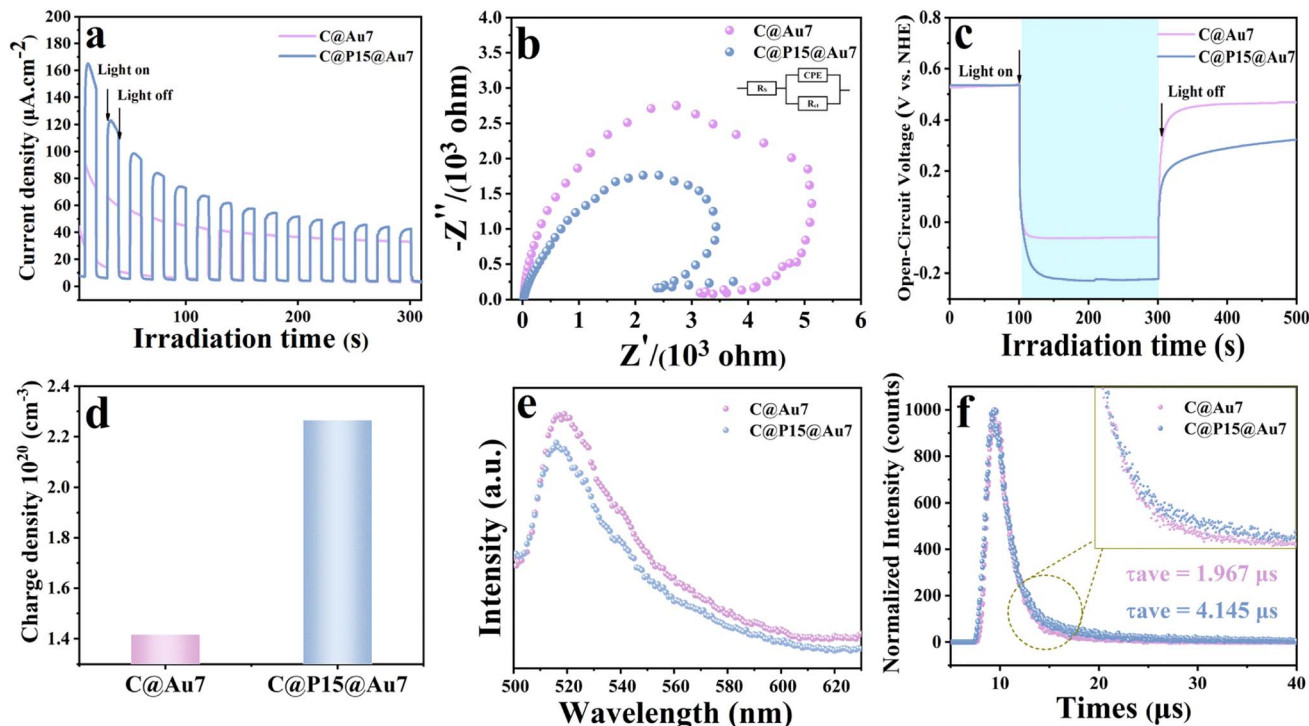


Fig. 6 (a) Photocurrent and (b) EIS Nyquist plots of C@Au7 and C@P15@Au7 under visible light ($\lambda > 420$ nm) irradiation in an aqueous Na₂SO₄ solution (0.5 M and pH = 6.69), (c) open-circuit potential decay, (d) charge carrier densities, (e) PL spectra, and (f) time-resolved transient PL decay.

PDDA layer can more effectively improve the charge migration compared to C@Au7. As exhibited in Fig. 6b, the smaller semicircular arc radius of C@P15@Au7 relative to that of C@Au7 indicates its smaller charge transfer resistance and higher charge separation efficiency.⁴³ Together with the simulated results (Table S8†), C@P15@Au7 (3158 ohm) exhibits smaller charge transfer resistance (R_{ct}) in comparison with C@Au7 (4698 ohm) under the same conditions, implying that the R_{ct} of C@P15@Au7 is greatly reduced with a PDDA layer intercalated in-between CdS and Au NCs. To explore the carrier recombination kinetics, open circuit photovoltage (OCVD) results of photo-electrodes were explored, which is deemed to be an effective tool to monitor the open circuit voltage (V_{oc}) decay upon turning off the light irradiation in a steady state. As revealed in Fig. 6c, C@P15@Au7 exhibits a larger photovoltage compared with C@Au7, which once again corroborates that more enhanced charge separation occurs over C@P15@Au7 with respect to C@Au7. Alternatively, Mott-Schottky (M-S) measurement provides a simple approach to determine the charge carrier density of photoelectrodes (Fig. 6d and S45†). The charge carrier density (N_D) of the photoelectrode can be calculated by using the following equation:

$$N_D = \left(\frac{2}{\epsilon_r \epsilon_0 e_0} \right) \left(\frac{d \left(\frac{1}{C^2} \right)}{dV} \right)^{-1} \quad (5)$$

where ϵ_r denotes the dielectric constant of the semiconductor ($\epsilon_{CdS} = 8.9$), ϵ_0 denotes the permittivity of vacuum (8.86×10^{-12} F m⁻¹), e_0 is the electronic charge unit (1.6×10^{-19} C), V is the potential applied on the electrode, and C is the capacitance. The N_D values of C@Au7 and C@P15@Au7 are determined to be 1.41×10^{20} and 2.26×10^{20} cm⁻³ (Fig. 6d), respectively, which verifies that C@P15@Au7 demonstrates larger charge transfer efficiency than C@Au7 on account of the strong electron-withdrawing ability of PDDA. Thus, PEC results indicate that incorporating an ultra-thin PDDA layer at the interfacial domain of CdS and Au@citrate NCs can boost the interfacial charge transfer efficiency, wherein the PDDA interim layer serves as an efficient electron transfer mediator.

In order to gain insight into the action mechanism of PDDA in photocatalytic reactions, charge transport processes of C@Au7 and C@P15@Au7 heterostructures were investigated by spectroscopic techniques. Fig. 6e and f record the photoluminescence (PL) and time-resolved photoluminescence (TRPL) decay curves of C@Au7 and C@P@Au7. In principle, the PL emission peak is the product of the radiative recombination of charge carriers in a material.⁴⁴ As exhibited in Fig. 6e, obviously, the PL quenching amplitude of C@P15@Au7 is larger than that of C@Au7, strongly suggesting that recombination of photogenerated carriers over C@P15@Au7 is remarkably inhibited. TRPL spectra are used to study the specific carrier dynamics of the photosystems. As displayed in Fig. 6f, fitting results reveal an average lifetime of 4.145 μs for C@P15@Au7 and 1.967 μs for C@Au7. The increase in the PL lifetime can be

explained by the decrease in the radiative recombination, which means that there are more carriers that are available to participate in the photocatalytic reaction.⁴⁵ There is no doubt that introducing PDDA as an interfacial interim layer can effectively suppress the carrier recombination.

3.5 Photocatalytic mechanism

The *in situ* XPS tool has been determined as an effective technique to analyze the surface chemistry and charge transport mechanism of photocatalysts.⁴⁶ The variation of element binding energy can directly reflect the change of electron density, where a positive shift in the binding energy of the core element suggests an electron density reduction and *vice versa*.⁴⁷ As shown in Fig. 7a and b, compared with C@P15@Au7 in the dark, the binding energy of Cd 3d and S 2p in C@P15@Au7 under light irradiation markedly moves to a higher energy level. Contrarily, the binding energy of Cl 2p in C@P15@Au7 obviously shifts to a lower energy level (Fig. 7c), suggesting photoelectron transfer from the CdS substrate to PDDA under light irradiation. The result confirms that PDDA possesses a strong electron-withdrawing ability. Besides, as displayed in Fig. 7d, the binding energy of Au 4f in C@P15@Au7 obviously shifts toward a lower energy level under visible light irradiation, meaning an increase in the electron density of Au@citrate NCs. Apparently, Au@citrate NCs accepts the photoelectrons relayed by PDDA, indicating that a unidirectional cascade charge transfer chain originating from the substrate (CdS) pointing to the electron reservoir (Au@citrate NCs) has been successfully constructed in our photosystem (Fig. 7e).

In order to unveil the interfacial carrier dynamics, ultrafast transient absorption (TA) spectroscopy as a robust tool was utilized to track the carrier dynamics in real time. Fig. 7f, i and S46† separately exhibit the 2D pseudo-color maps of TA spectra at 400 nm excitation and TA spectra profiles taken at several representative time delays of C@Au7 and C@P@Au7 heterostructures. The negative ΔOD bleaching signal is attributed to the well-known band filling effect.⁴⁸ Fig. 7g and j compare the kinetics trace of C@Au7 and C@P@Au7, which can be fitted with biexponential and tri-exponential decay functions, respectively. Generally, different decay durations indicate the consecutive pathway of electron relaxation to different trap states with diverse trap depths.⁴⁸ In our work, as for C@P15@Au7, the relaxation time implies electron transfer (ET) from the conduction band (CB) minimum to a shallow trap state Trap1 and then to a deep trap state Trap2, and recombine with the holes (Trap3), featuring the different decay times of τ_1 , τ_2 and τ_3 , respectively. The carrier transport process is illustrated in Fig. 7h and k. In terms of the electron relaxation time τ_1 , the time corresponding to C@P15@Au7 is 66.8 ps, which is significantly shorter than that of C@Au7 (108.26 ps). The shorter the relaxation time, the faster the electron transfer rate, and thus this phenomenon intuitively and powerfully confirms that PDDA can act as an electron-relay mediator in the kinetics process. Apparently, PDDA can capture electrons from the CdS substrate more efficiently than Au@citrate NCs. In addition, as for C@Au7 and C@P15@Au7, relaxation times for electrons

falling back from Au@citrate NCs to the CB of CdS are 532.40 and 711.99 ps, respectively. Notably, the longer electron residing time over Au@citrate NCs means that the electron supply quantity increases, and more electrons can participate in the reaction. The above analysis confirms that introducing an ultrathin PDDA interim layer into the C@P15@Au7 heterostructure effectively activates the interfacial charge transport kinetics, and we believe that a unidirectional cascade charge transport channel can be precisely and efficiently constructed to accelerate electron transport with the synergistic effect of PDDA and Au@citrate NCs.

In light of the above analysis, the photocatalytic mechanisms of the C@P15@Au heterostructure are illustrated in Scheme 2. According to the M-S results (Fig. S47a†), the flat band potential (E_{fb}) of CdS is determined to be -0.6 V vs. NHE, and considering that the E_{fb} of n-type semiconductors is more positive by 0.1 V than the CB potential (E_{CB}), the E_{CB} of CdS is calibrated to be -0.7 V vs. NHE. Since the band gap of CdS is 2.39 eV based on the DRS result (Fig. S47b†), the valence band (VB) potential (E_{VB}) of CdS is calculated to be 1.69 V vs. NHE. The energy band structure of CdS is shown in Fig. S47c.† Due to the uneven distribution of space charge, pristine CdS is prone to form a built-in electric field, which is not conducive to the photoelectron transfer from the CdS matrix to the surface, thus seriously limiting the photocatalytic activity (Fig. S48†).⁴⁹ Noteworthy, the ultrathin intermediate PDDA layer as an electron traction “pump” in the C@P@Au heterostructure demonstrates powerful electron-withdrawing ability, which can extract the electrons enriched on the CdS surface in time, thus effectively eliminating the detrimental influence of the built-in electric field. At the same time, Au@citrate NCs act as terminal “electron reservoirs” to rapidly receive the electrons relayed from the PDDA interim layer. In this regard, an efficient vectorial cascade charge transport chain is constructed between CdS and Au@citrate NCs with the assistance of PDDA (Fig. S48†). Specifically, CdS is photoexcited under visible light irradiation to produce electron-hole pairs with electrons flowing to the CB, leaving holes in the VB. Subsequently, the intermediate PDDA layer functions as an electron-withdrawing mediator to draw electrons from the CB of CdS and then accelerates the unidirectional electron transport to terminal Au@citrate NCs. Subsequently, the electrons aggregating on the surface of Au@citrate NCs initiate multifarious photoredox catalysis: (1) electrons trigger proton reduction to produce H_2 ($2e^-$), while holes residing in the VB of CdS are quenched by the electron donor (lactic acid); (2) as important active species, electrons and protons synergistically coordinate to participate in the multi-step coupling to form azo intermediates (Fig. S49†) and finally promote the photoreduction of aromatic nitro compounds to amino derivatives ($6e^-$). Concurrently, holes remaining in the VB of CdS are quenched by the electron donor (ammonium formate); (3) electrons react with the activated CO_2 to produce $CO_2^{\cdot-}$ radicals with the involvement of proton and electron transfer, wherein the C–O bond breaks to generate CO ($CO_2 + 2H^+ + 2e^- \rightarrow CO + H_2O$) and CH_4 ($CO_2 + 8H^+ + 8e^- \rightarrow CH_4 + 2H_2O$) along the route $CO_2^{\cdot-} \rightarrow CO \rightarrow C \cdot \rightarrow CH_3 \cdot \rightarrow CH_4$ (Fig. S50†).⁵⁰ Simultaneously, holes remaining in the VB of CdS



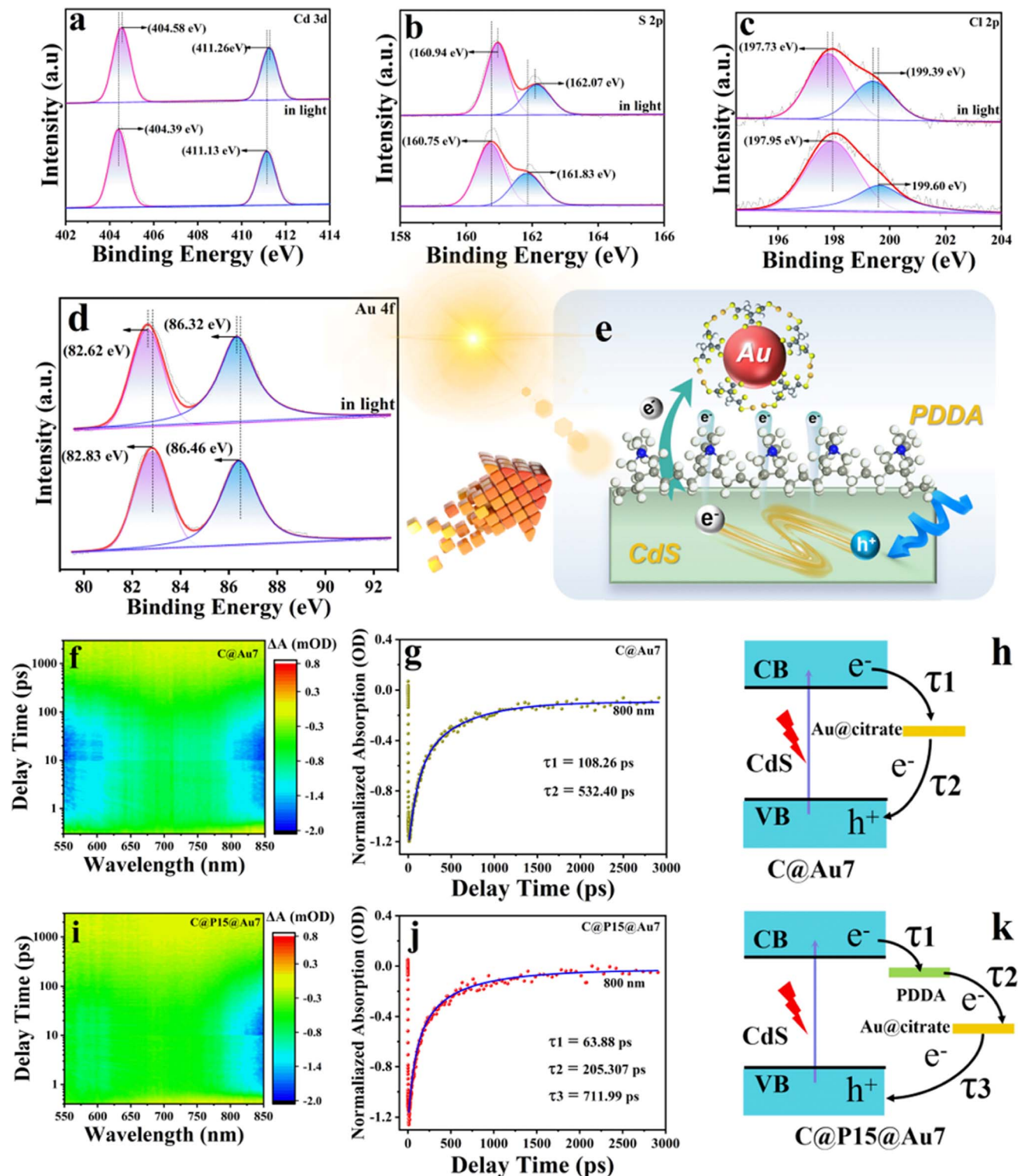
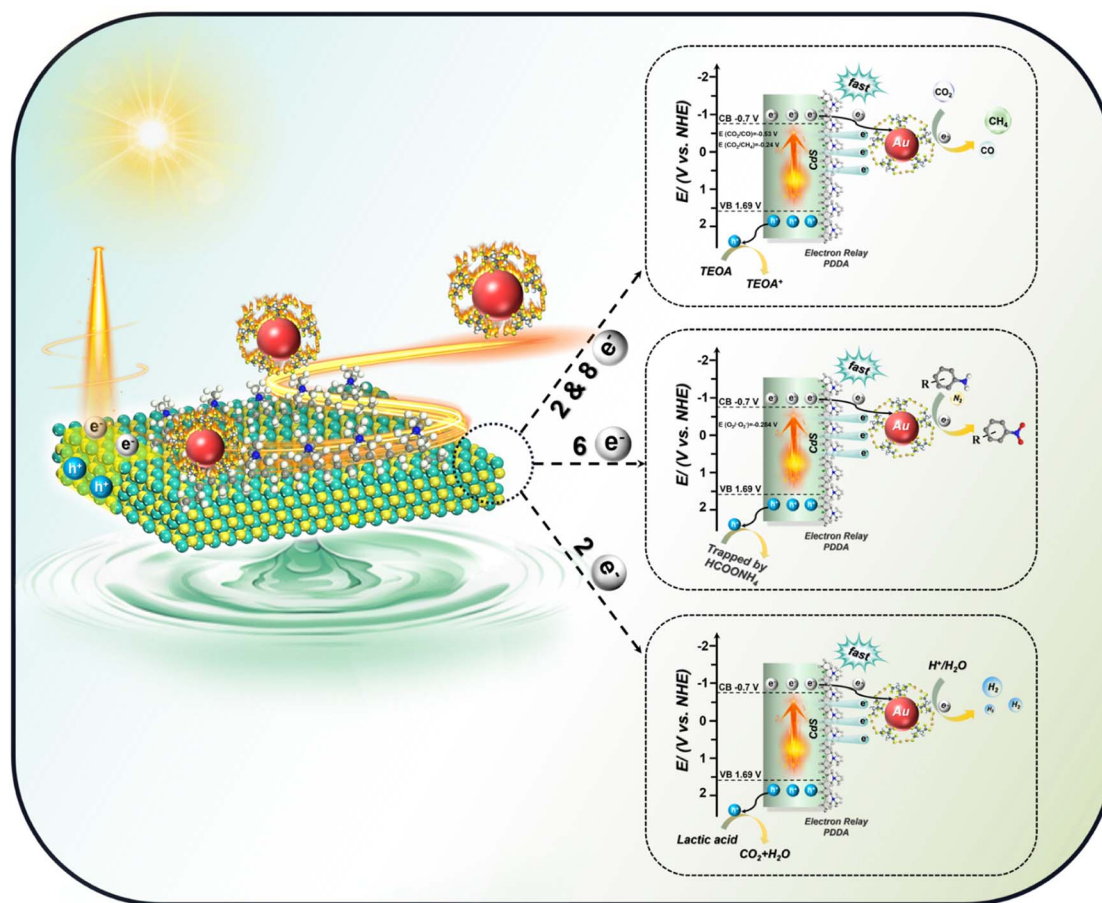


Fig. 7 *In situ* irradiated high-resolution spectra of (a) Cd 3d, (b) S 2p, (c) Cl 2p and (d) Au 4f for C@P15@Au7, (e) schematic diagram of photoelectron transfer over the C@P15@Au7 heterostructure, (f and i) 2D pseudo-color maps of TA spectra under 400 nm excitation, (g and j) relaxation kinetics measured at a probing wavelength of 800 nm for C@Au7 and C@P15@Au7, and (h and k) schematic diagrams of the possible charge transfer mechanisms.

are also quenched by the electron donor (TEOA); (4) electrons combine with the dissolved oxygen in the reaction system to generate two primary oxidation active species including $\cdot OH$

and $\cdot O_2^-$ radicals that synergistically trigger the photocatalytic selective oxidation of aromatic alcohols to aldehydes by deprotonation processes (Fig. S51†). It should be emphasized



Scheme 2 Schematic illustration of the photocatalytic mechanisms of the C@P@Au heterostructure.

that even under more severe triggering conditions, PDDA-mediated vectorial charge transport chains still retain inexhaustible electron transport capability. Furthermore, more intriguingly, it was evidenced that the PDDA mediated unidirectional charge transfer model (CdS@PDDA@M) is universal for a large variety of noble metals (M: Au, Ag, Pt), non-noble metals (M: Ni, Co, Cu) and semiconductor (M: NiSe₂, CoSe₂, CuSe) reducing co-catalysts as terminal “electron reservoirs”.

4. Conclusions

In summary, we conceptually constructed a novel cascade charge transport chain over a transition metal chalcogenide (CdS) by introducing an ultrathin non-conjugated insulating polymer (PDDA) layer at the interface *via* a progressive self-assembly strategy for multifarious photoredox catalysis. We found that such an ultrathin intermediate PDDA layer demonstrates powerful electron-withdrawing ability for relaying electrons between the CdS substrate and terminal electron reservoirs, considerably accelerating the interfacial charge transfer kinetics towards multifarious visible-light-driven photoredox reactions including photocatalytic hydrogen generation, anaerobic photocatalytic organic transformation (aromatic nitro compound reduction and aromatic alcohol oxidation), and photocatalytic CO₂-to-fuel conversion.

Furthermore, the PDDA mediated unidirectional charge transfer model (CdS@PDDA@M) is universal for diverse noble metals (M: Au, Ag, Pt), non-noble metals (M: Ni, Co, Cu) and semiconductor (M: NiSe₂, CoSe₂, CuSe) reducing co-catalysts. Our work would provide a novel and feasible way to finely regulate unexpected charge flow *via* insulating polymers for solar energy conversion.

Data availability

The datasets supporting this article have been uploaded as part of the ESI.†

Author contributions

Xian Yan performed the experiments, analyzed all data, and draft the manuscript. Jun-Hao Dong carried out and analyzed the TA experiments. Fang-Xing Xiao guided this work and correct the manuscript. Jing-Ying Zheng and Yue Wu help to check the manuscript. All the authors contributed to a critical discussion on the data and the manuscript.

Conflicts of interest

The authors declare no competing interests.



Acknowledgements

The support by the award program for Minjiang scholar professorship is greatly acknowledged. This work was financially supported by the National Natural Science Foundation of China (No. 21703038 and 22072025).

References

- 1 Y. Liu, M. Zhang, Z. Wang, J. He, J. Zhang, S. Ye, X. Wang, D. Li, H. Yin, Q. Zhu, H. Jing, Y. Weng, F. Pan, R. Chen, C. Li and F. Fan, *Nat. Commun.*, 2022, **13**, 4245.
- 2 X. Tao, Y. Zhao, S. Wang, C. Li and R. Li, *Chem. Soc. Rev.*, 2022, **51**, 3561–3608.
- 3 D. E. McCoy, T. Feo, T. A. Harvey and R. O. Prum, *Nat. Commun.*, 2018, **9**, 1.
- 4 P. Prabhu, V. Jose and J. M. Lee, *Adv. Funct. Mater.*, 2020, **30**, 1910768.
- 5 J. S. Lee, D. I. Won, W. J. Jung, H. J. Son, C. Pac and S. O. Kang, *Angew. Chem., Int. Ed.*, 2017, **56**, 976–980.
- 6 X.-C. Dai, M.-H. Huang, Y.-B. Li, T. Li, B.-B. Zhang, Y. He, G.-C. Xiao and F.-X. Xiao, *J. Mater. Chem. A*, 2019, **7**, 2741–2753.
- 7 K.-Y. Jiang, Y.-L. Weng, S.-Y. Guo, Y. Yu and F.-X. Xiao, *Nanoscale*, 2017, **9**, 16922–16936.
- 8 L. Cheng, Q. Xiang, Y. Liao and H. Zhang, *Energy Environ. Sci.*, 2018, **11**, 1362–1391.
- 9 F.-X. Xiao and B. Liu, *Adv. Mater. Interfaces*, 2018, **5**, 1701098.
- 10 Z. Zeng, F.-X. Xiao, H. Phan, S. Chen, Z. Yu, R. Wang, T.-Q. Nguyen and T. T. Yang Tan, *J. Mater. Chem. A*, 2018, **6**, 1700–1713.
- 11 A. Singh and A. S. K. Sinha, *Appl. Surf. Sci.*, 2018, **430**, 184–197.
- 12 T. Li, M.-H. Huang, Y.-B. Li, X.-C. Dai, Y. He, G. Xiao and F.-X. Xiao, *J. Mater. Chem. A*, 2019, **7**, 21182–21194.
- 13 H. Zhu, N. Song, W. Rodriguez-Cordoba and T. Lian, *J. Am. Chem. Soc.*, 2012, **134**, 4250–4257.
- 14 B. Tang, S.-C. Zhu, H. Liang, S. Li, B.-J. Liu and F.-X. Xiao, *J. Mater. Chem. A*, 2022, **10**, 4032–4042.
- 15 Z. Zhang, Y. Huang, K. Liu, L. Guo, Q. Yuan and B. Dong, *Adv. Mater.*, 2015, **27**, 5906–5914.
- 16 S. Hou, M.-H. Huang and F.-X. Xiao, *J. Mater. Chem. A*, 2022, **10**, 7006–7012.
- 17 A. R. Johnston, S. L. Perry and A. L. Ayzner, *Chem. Mater.*, 2021, **33**, 1116–1129.
- 18 Y. Xiao, Q.-L. Mo, G. Wu, K. Wang, X.-Z. Ge, S.-R. Xu, J.-L. Li, Y. Wu and F.-X. Xiao, *J. Mater. Chem. A*, 2023, **11**, 2402–2411.
- 19 X. Ouyang, R. Peng, L. Ai, X. Zhang and Z. Ge, *Nat. Photonics*, 2015, **9**, 520–524.
- 20 Q.-L. Mo, J. L. Li, S. R. Xu, K. Wang, X. Z. Ge, Y. Xiao, G. Wu and F.-X. Xiao, *Adv. Funct. Mater.*, 2023, **33**, 2210332.
- 21 Q.-L. Mo, X. Lin, Z.-Q. Wei, X.-C. Dai, S. Hou, T. Li and F.-X. Xiao, *J. Mater. Chem. A*, 2020, **8**, 16392–16404.
- 22 S. Li, Q. L. Mo, S. C. Zhu, Z. Q. Wei, B. Tang, B. J. Liu, H. Liang, Y. Xiao, G. Wu, X. Z. Ge and F.-X. Xiao, *Adv. Funct. Mater.*, 2022, **32**, 2110848.
- 23 C. Dai and B. Liu, *Energy Environ. Sci.*, 2020, **13**, 24–52.
- 24 F. Xiao, *J. Phys. Chem. C*, 2012, **116**, 16487–16498.
- 25 Q. Zhang, Q. An, X. Luan, H. Huang, X. Li, Z. Meng, W. Tong, X. Chen, P. K. Chu and Y. Zhang, *Nanoscale*, 2015, **7**, 14002–14009.
- 26 Y. Wang, F. Chen, W. Yu and L. Zhao, *Chem. Eng. J.*, 2021, **413**, 127543.
- 27 S. Rengaraj, S. Venkataraj, S. H. Jee, Y. Kim, C. W. Tai, E. Repo, A. Koistinen, A. Ferancova and M. Sillanpaa, *Langmuir*, 2011, **27**, 352–358.
- 28 K. Ojha, T. Debnath, P. Maity, M. Makkar, S. Nejati, K. V. Ramanujachary, P. K. Chowdhury, H. N. Ghosh and A. K. Ganguli, *J. Phys. Chem. C*, 2017, **121**, 6581–6588.
- 29 J. Ma, H. Chi, A. Wang, P. Wang, H. Jing, T. Yao and C. Li, *J. Am. Chem. Soc.*, 2022, **144**, 17540–17548.
- 30 S. Zhao, Y. Zhang, Y. Zhou, C. Zhang, X. Sheng, J. Fang and M. Zhang, *ACS Sustain. Chem. Eng.*, 2017, **5**, 1416–1424.
- 31 Q.-L. Mo, S.-R. Xu, J.-L. Li, X.-Q. Shi, Y. Wu and F.-X. Xiao, *Small*, 2023, **19**, 2300804.
- 32 B. Lin, H. Li, H. An, W. Hao, J. Wei, Y. Dai, C. Ma and G. Yang, *Appl. Catal., B*, 2018, **220**, 542–552.
- 33 M. Q. Yang, Y. J. Xu, W. Lu, K. Zeng, H. Zhu, Q. H. Xu and G. W. Ho, *Nat. Commun.*, 2017, **8**, 14224.
- 34 Q.-L. Mo, X.-C. Dai and F.-X. Xiao, *Small*, 2023, **19**, 2302372.
- 35 S. Xu, M.-H. Huang, T. Li, Z.-Q. Wei, X. Lin, X.-C. Dai, S. Hou, X.-Y. Fu and F.-X. Xiao, *J. Mater. Chem. A*, 2020, **8**, 8360–8375.
- 36 Y. X. Feng, H. J. Wang, J. W. Wang, W. Zhang, M. Zhang and T. B. Lu, *ACS Appl. Mater. Interfaces*, 2021, **13**, 26573–26580.
- 37 S.-C. Zhu, Z. Wang, B. Tang, H. Liang, B.-J. Liu, S. Li, Z. Chen, N. Cheng and F.-X. Xiao, *J. Mater. Chem. A*, 2022, **10**, 11926–11937.
- 38 Y.-B. Li, T. Li, X.-C. Dai, M.-H. Huang, S. Hou, X.-Y. Fu, Z.-Q. Wei, Y. He, G. Xiao and F.-X. Xiao, *ACS Appl. Mater. Interfaces*, 2020, **12**, 4373–4384.
- 39 C. Bie, B. Zhu, F. Xu, L. Zhang and J. Yu, *Adv. Mater.*, 2019, **31**, 1902868.
- 40 Z. Q. Wei, S. Hou, S. C. Zhu, Y. Xiao, G. Wu and F.-X. Xiao, *Adv. Funct. Mater.*, 2022, **32**, 2106338.
- 41 B. Wang, J. Zhao, H. Chen, Y.-X. Weng, H. Tang, Z. Chen, W. Zhu, Y. She, J. Xia and H. Li, *Appl. Catal., B*, 2021, **293**, 120182.
- 42 X. Lin, S. Xu, Z.-Q. Wei, S. Hou, Q.-L. Mo, X.-Y. Fu and F.-X. Xiao, *J. Mater. Chem. A*, 2020, **8**, 20151–20161.
- 43 A. P. Singh, N. Kodan, B. R. Mehta, A. Held and L. Mayrhofer, *ACS Catal.*, 2016, **6**, 5311–5318.
- 44 X. Yue, S. Yi, R. Wang, Z. Zhang and S. Qiu, *Nano Energy*, 2018, **47**, 463–473.
- 45 S. Nayak, L. Mohapatra and K. Parida, *J. Mater. Chem. A*, 2015, **3**, 18622–18635.
- 46 L. Wang, B. Cheng, L. Zhang and J. Yu, *Small*, 2021, **17**, 2103447.
- 47 X. Yan, X.-Y. Fu and F.-X. Xiao, *Adv. Funct. Mater.*, 2023, **33**, 2303737.
- 48 X. Lu, A. Tong, D. Luo, F. Jiang, J. Wei, Y. Huang, Z. Jiang, Z. Lu and Y. Ni, *J. Mater. Chem. A*, 2022, **10**, 4594–4600.
- 49 R. Chen, F. Fan, T. Dittrich and C. Li, *Chem. Soc. Rev.*, 2018, **47**, 8238–8262.
- 50 L. Cheng, B.-H. Li, H. Yin, J.-J. Fan and Q.-J. Xiang, *J. Mater. Sci. Technol.*, 2022, **118**, 54–63.

